

Atmospheric effects on low elevation transmission measurements at EOPACE

J. Luc Forand^a, Mike Duffy^a, Carl Zeisse^b, Stewart Gathman^c, Arie de Jong^d, and Denis Dion^a

^aDefence Research Establishment Valcartier
2459 Pie XI Blvd. N., Val-Belair, QC, Canada G3J 1X5

^bPropagation Division, NCCOSC RDTE DIV 883
49170 Propagation Path, San Diego, CA, USA 92152-7385

^cOcean and Atmospheric Sciences Division, NCCOSC RDTE DIV 543
53170 Woodward Road, San Diego, CA, USA 92152-7385

^dTNO Physics and Electronics Laboratory
P.O. Box 96864, 2509 JG The Hague, The Netherlands

ABSTRACT

An analysis is presented showing the effects of refraction, aerosol extinction, and molecular extinction on transmission measurements obtained during the EO Propagation Assessment in Coastal Environments (EOPACE) campaign carried out in San Diego during March and April 1996. Infrared transmission measurements were made over both a 7 km path (mid IR) and a 15 km path (mid IR and far IR) at heights below 10 m above sea level. The average difference between all the measured transmissions and aerosol transmittances over the two paths with results obtained using the IR Boundary Layer Effects Model (IRBLEM) were found to be relatively small, even though the difference for individual measurements can be significant. The effect of molecular transmittance, as calculated using MODTRAN, is found to reduce the transmission by about 35% for the 7 km path, 72% for the mid IR over the 15 km path, and between 70% and 90% for the far IR over the 15 km path. The effect of aerosol transmittance, as calculated using a variation of the Navy Aerosol Model (NAM), is found to reduce the transmission from 10% to 90% for the mid IR over both the 7 and 15 km paths, and from 10% to 60% for the far IR over the 15 km path. The effect of refractance, the focussing and defocussing of radiation due to atmospheric refraction, on the predicted transmissions is found to account for gains and losses up to 20% for the 7 km path, and gains and losses up to 100% for the 15 km path. Consequently, any IR transmission model for the marine boundary layer (MBL) must properly take into account the effects on the transmission due to molecular extinction, aerosol extinction, and refractance.

Keywords: refraction, atmospheric transmission, marine boundary layer, molecular extinction, aerosol extinction, EOPACE

1. INTRODUCTION

The intensive operational period (IOP) of the EO Propagation Assessment in Coastal Environments (EOPACE) campaign that was conducted in San Diego during March and April 1996, was a good opportunity to obtain excellent transmission data within the marine boundary layer (MBL) and to compare it to predictions made by the IR Boundary Layer Effects Model (IRBLEM). This was made possible due to the good quality of the mid-infrared (MIR) transmission data obtained by Carl Zeisse of NRaD over his 7 km transmission path, the MIR and far-infrared (FIR) transmission data obtained by Arie de Jong of TNO over his 15 km transmission path, the basic meteorological data obtained at both ends and in the middle of each transmission path, and the measurement of the aerosol size distribution over both transmission paths by Stewart Gathman of NRaD.

To better understand how the data was obtained and how the analysis was performed using IRBLEM¹, the following section presents a brief discussion of the effects which can affect the transmission of IR radiation in the MBL and the modules that IRBLEM uses to model them. The following section gives a short description of the various meteorological and transmission equipment that was used and its location around San Diego Bay. The last three sections present the results of the study, a

Further author information -

Email: Luc.Forand@drev.dnd.ca; WWW:<http://www.drev.dnd.ca>; Tel.:(418)-844-4503; Fax: (418)-844-4511

discussion of the results, and finally some conclusions.

2. IR TRANSMISSION IN THE MARINE BOUNDARY LAYER

The marine boundary layer (MBL) is a region of the atmosphere which extends from the marine surface to a height which may vary from 20 to several 100 meters. As the air and marine surface can often be at different temperatures, this region of the atmosphere, through convection and air transport, can possess strong vertical gradients of temperature, humidity, and aerosol concentration. The MBL is also a region that is a source of maritime aerosols and a sink, particularly in coastal regions, for terrestrial aerosols (particulates). The various gradients, the concentrations, type and particle distribution of the aerosols, and the amount of water vapour in the MBL all have important consequences on the transmission of IR radiation. The gradients can cause significant refractive effects (mirage formation, focussing and defocussing), while the composition of the MBL determines the amount of IR radiation that is scattered or absorbed.

For a spherical wavefront of frequency, ν , the intensity, $I(\mathbf{r}, \nu)$, at some vector position, \mathbf{r} , from a point source can be expressed by:

$$I(\mathbf{r}, \nu) = \frac{I_0(\nu)}{r^2} \sum_{j=1}^m \rho_j(\mathbf{r}, \nu) \tau_{jM}(\mathbf{r}, \nu) \tau_{jA}(\mathbf{r}, \nu) = \frac{I_0(\nu)}{r^2} \sum_{j=1}^m T_j(\mathbf{r}, \nu) = \frac{I_0(\nu)}{r^2} T(\mathbf{r}, \nu), \quad (1)$$

where m is the number of images (m is greater than 1 when there are secondary images or mirages), j is an image index,

$$T(\mathbf{r}, \nu) = \sum_{j=1}^m T_j(\mathbf{r}, \nu) = \sum_{j=1}^m \rho_j(\mathbf{r}, \nu) \tau_{jM}(\mathbf{r}, \nu) \tau_{jA}(\mathbf{r}, \nu) \quad (2)$$

is the total transmission, and

$$\tau_{jx}(\mathbf{r}, \nu) = e^{-\int_0^r \alpha_x(\mathbf{r}(s), \nu) ds_j}; \text{ for } x = M, A \quad (3)$$

is either the molecular transmittance, $\tau_{jM}(\mathbf{r}, \nu)$, or the aerosol transmittance, $\tau_{jA}(\mathbf{r}, \nu)$, and the integral is taken over the path followed by the ray creating the image and the respective extinction coefficient, $\alpha_x(\mathbf{r}, \nu)$. $I_0(\nu)$ is the total emitted intensity and $\rho(\mathbf{r}, \nu)$ is the refractance at the vector position, \mathbf{r} for frequency, ν . For straight rays (i.e., no refraction) the refractance equals 1; however, if the rays are focussed, the refractance becomes greater than 1, and if they are defocussed, the refractance becomes less than 1. Thus, the refractance can be thought of as an optical amplifier with a gain of ρ .

The IR Boundary Layer Effects Model (IRBLEM)¹ has been designed to calculate each of the above terms for rays which propagate within the MBL. Figure 1 shows the internal modular structure of IRBLEM with the meteorological inputs situated at the top and the various outputs at the bottom. The required meteorological data is passed to each of the four subsequent routines which calculate the molecular extinction ($\tau_M(\nu)$), the vertical refractivity profile ($N(h)$), the vertical refractivity structure parameter profile ($C_n^2(h)$; turbulence), and the vertical aerosol extinction profile ($\alpha_A(h)$). The molecular extinction is spectrally calculated using a call to MODTRAN² in the horizon mode for the height at which the air temperature was measured, the desired wavelength band, and for a nominal resolution of 5 cm⁻¹. The molecular extinction is not height dependent. The vertical structure parameter profile, which was not required for this study, is calculated using SRS_BULK³ and is not discussed any further. For the calculation of the vertical aerosol extinction coefficient profile, a module was provided by TNO¹, that allows the user to select one of three models to estimate the aerosol extinction at 10 m's above the surface for a wavelength of either 4 μm (center of the 3-5 μm waveband) or 10 μm (center of the 8-12 μm waveband). The model choices are the Navy Aerosol Model⁴ (NAM), the Open Ocean⁵ model, and the TNO MPN⁶ model. The vertical variation is computed after de Leeuw⁷ using LKB⁸ for estimating the characteristic MBL parameters and assuming that the vertical distribution for all particle sizes follows that for the 1 micron particles. Calculation of the vertical refractivity profile is carried out using subroutines taken from DREV's LWKWD⁹ model that makes calculations for the mid IR and far IR bands. It is an MBL model that is based upon the similarity theory work of Monin and Obukhov¹⁰. The results of these calculations are then passed to a DREV developed ray-tracing program¹ that is

capable of calculating the change in the intensity along any ray due to lensing effects (the refractance) using a technique developed by Blanchard¹¹, and calculates the molecular transmittance and aerosol transmittance by performing the integral in Eq. 3 over each ray.

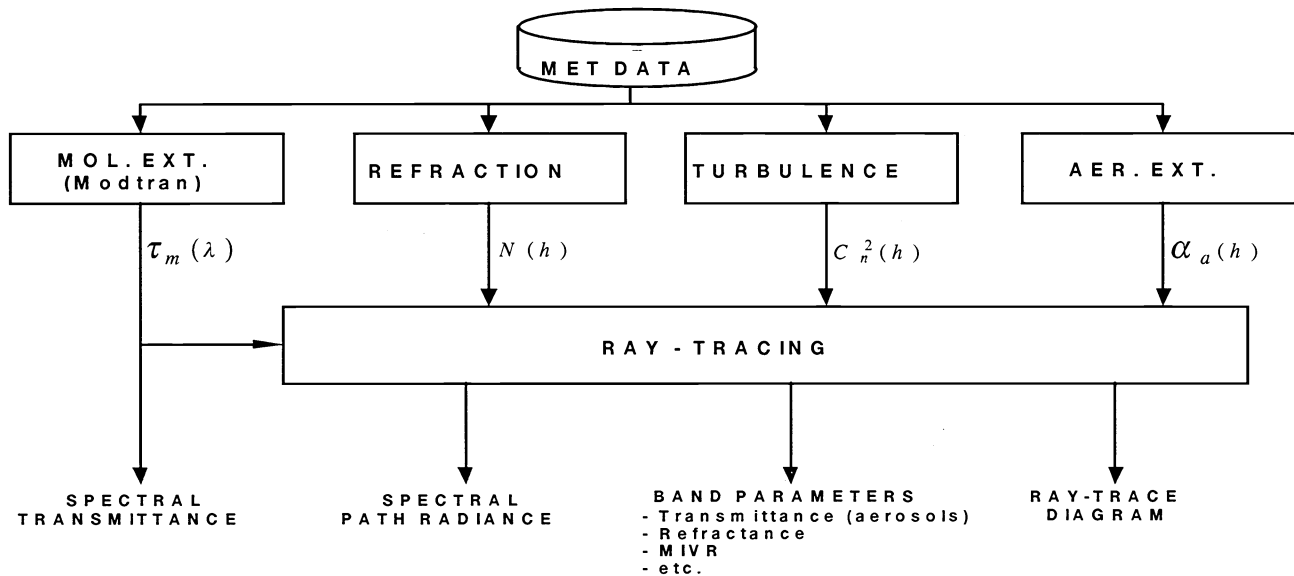


Figure 1 - Schematic diagram showing the modular structure of IRBLEM.

3. EXPERIMENTAL DETAILS

Figure 2 shows a map of Southern California and San Diego Bay which indicates the sites where the various equipment was used during EOPACE's intensive operational period (IOP) of March-April, 1996. The Naval Postgraduate School in Monterey had positioned a "MEAN" weather buoy at the midpoint of the 7 km transmission path (between the Subbase and Coronado), and a "FLUX" weather buoy at the midpoint of the 15 km transmission path (between the Subbase and the pier at Imperial Beach). Both buoys made continuous measurements of the air temperature, water temperature, relative humidity, atmospheric pressure, wind speed and direction during most of the IOP. The FLUX buoy also made measurements of the wave spectra and their amplitudes. TNO had meteorological stations placed at both ends of the 15 km path where they measured the relative humidity, air temperature, atmospheric pressure, wind speed and direction. Similarly, NRaD had meteorological stations placed at both ends of the 7 km path where they measured the air temperature, relative humidity, wind speed and direction. The visibility was also measured continuously at the Subbase by either DREV or NRaD, and measurements of irradiance, condensation nuclei (CN), and radon were taken by NRaD out at Pt. Loma. The air temperature, water temperature and relative humidity were also obtained almost once a day, over each of the transmission paths by a small boat operated by NRaD. NRaD also measured the aerosol size distribution from the boat and used Mie theory to calculate aerosol extinction coefficients for 3.5 μm and 10.6 μm.

To properly compare the waveband transmission measurements, over the different paths, with the spectrally dependent (every 5 cm⁻¹) predictions from IRBLEM, the predictions must be weighted by the weighting function, $w(\nu)$, over the appropriate waveband (weighted average). The total waveband transmission, $T(\nu_{\min}, \nu_{\max})$, between the frequencies ν_{\min} and ν_{\max} , can be expressed by;

$$T(\nu_{\min}, \nu_{\max}) = \int_{\nu_{\min}}^{\nu_{\max}} w(\nu) T(\nu) d\nu = \sum_{j=1}^m \int_{\nu_{\min}}^{\nu_{\max}} w(\nu) T_j(\nu) d\nu \approx \sum_{j=1}^m \rho_j(\nu_b) \tau_{jA}(\nu_b) \int_{\nu_{\min}}^{\nu_{\max}} w(\nu) \tau_{jM}(\nu) d\nu = \sum_{j=1}^m \rho_j(\nu_b) \tau_{jA}(\nu_b) T_{jM}, \quad (4)$$

where $T(\nu)$ is the total transmission given by Eq. 2, and $\rho(\nu_b)$ and $\tau_A(\nu_b)$ are the refractance and aerosol transmittance for the waveband, as produced by IRBLEM, respectively. (Note: the vector position, \mathbf{r} , has been suppressed for clarity.) T_{jM} is the

molecular transmittance for the waveband and the j^{th} image, and is given by:

$$T_{jM} = \int_{\nu_{\min}}^{\nu_{\max}} w(\nu) \tau_{jM}(\nu) d\nu = \sum_{i=0}^n w(\nu_{\min} + i\Delta\nu) \tau_{jM}(\nu_{\min} + i\Delta\nu) \Delta\nu = \sum_{i=0}^n w_i \tau_{ijM} \Delta\nu; \quad n = (\nu_{\max} - \nu_{\min}) / \Delta\nu - 1, \quad (5)$$

where the integral has been replaced by a summation over n frequency intervals, $w_i = w(\nu_{\min} + i\Delta\nu)$, and $\tau_{ijM} = \tau_{jM}(\nu_{\min} + i\Delta\nu)$. Finally, assuming that the source emission is spatially uniform (i.e., I_0 is independent of angle), the frequency dependent weighting function, $w(\nu)$, can be expressed as a function of the emission, $I_0(\nu, T)$, of the transmissometer's source, the temperature of the source, T , and the response, ϵ , of its detector by:

$$w(\nu) = \frac{I_0(\nu, T) \epsilon(\nu)}{\int_{\nu_{\min}}^{\nu_{\max}} I_0(\nu, T) \epsilon(\nu) d\nu}; \quad w_i = \frac{I_{0i}(T) \epsilon_i}{\sum_{i=0}^n I_{0i}(T) \epsilon_i \Delta\nu} \quad (6)$$

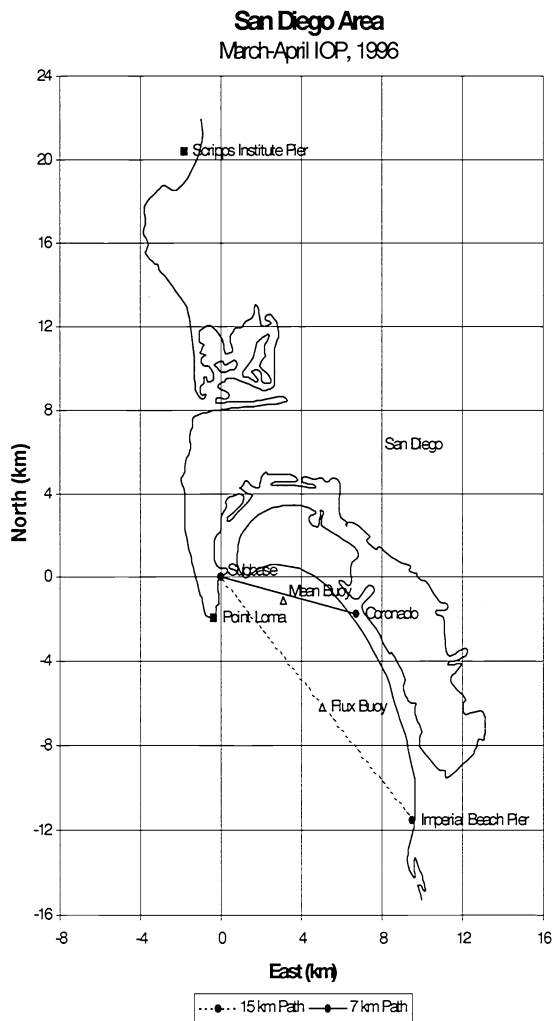


Figure 2 - Map of San Diego Bay and Southern California from Mexico to the Scripps Institute of Oceanography.

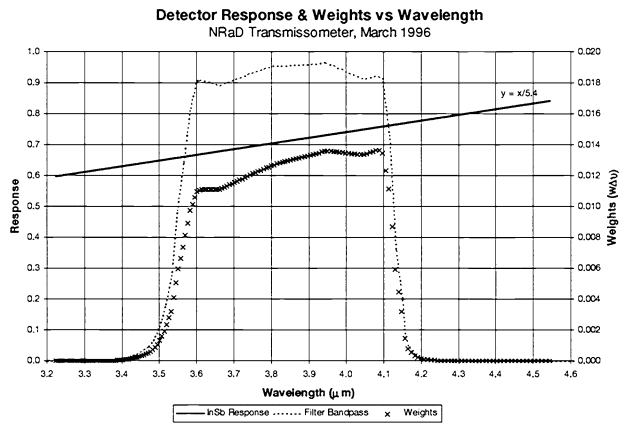


Figure 3 - Response of the InSb photon counter and the narrow band filter along with the calculated weights assuming an 800°C blackbody source and constant flux.

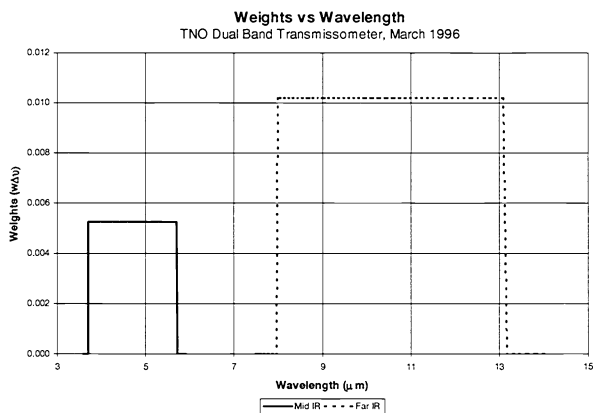


Figure 4 - Calculated weights for the mid-IR and far-IR bands assuming no frequency dependence between the appropriate 50% bandwidths.

The transmission measurements, taken with NRaD's transmissometer¹² over the 7 km path, were obtained using a wire coil emitter assumed to have a black body temperature of 800 °C, and a detector composed of an InSb photon counter (5.4 μm bandgap) in combination with a narrow band filter centered on the mid-infrared band. Both the source and receiver collimators had 20 cm diameter apertures and 1.2 m focal lengths (F/6). Figure 3 shows the response of both detector components and the calculated weights ($w\Delta v$) for the system. The TNO transmissometer^{12,13}, used over the 15 km path, was a dual band system which could be alternately operated in either the mid-infrared (50% bandwidths at 3.7 and 5.7 μm) or the far-infrared (50% bandwidths at 8.0 and 13.1 μm) wavelength band. However, as the response of the detectors and the temperature of the source was not known during the study, average ($w(v)$ constant) weighting functions were used over the 50% bandwidths for each band (see Fig. 4).

4. RESULTS

The first six graphs (Figs. 5a,b,c and Figs. 6a,b,c) are designed to give the reader an idea of the range of boundary layer conditions that were treated in this study over both the 7 km path and the 15 km path, respectively. The data points in each graph correspond to periods during which aerosol measurements were being taken by the small by boat (usually mid-morning or mid-afternoon), during the early morning (near 1300 GMT) when the air temperature was near its daily minimum, or during the late afternoon (near 2400 GMT) when the air temperature was near its daily maximum. For these periods (see Figs. 5a and 6a), the diurnal variations in the air temperature were from 23 °C, during the Santa Anna event (warm air mass) between April 6th and April 8th, to 12 °C at dawn. During the same period the water temperature varied slightly each day, and only varied between 14 and 16 °C during the two week IOP. As a result, the study contained ASTDs from -4 °C to +7 °C! Figs. 5c and 6c show that the wind also behaved diurnally, in that it generally came from the northeast in the late afternoon at 6 to 7 m/s, and from the south or east in the early morning at 2 to 4 m/s. The relative humidity and visibility (see Figs. 5b and 6b) also show diurnal behaviour. In general the visibility is better in the late evening than it is in the early morning, and the relative humidity is greater in the early morning than it is in the late afternoon. The one noticeable exception to this pattern occurred during the Santa Anna event.

Figures 7a-i, Figs. 8a-i, and Figs. 9a-i show various results of the study for the mid IR transmission measurements taken over the 7 km path, the mid IR transmission measurements taken over the 15 km path, and the far IR transmission measurements taken over the 15 km path, respectively. Before describing these graphs, the various calculation modes that are used are described below:

- A. The refractance or the aerosol transmittance are calculated using IRBLEM. They are band averages and have no spectral dependence within the band.
- B. The molecular transmittance and the total transmission for a waveband are calculated using IRBLEM and then either averaging the results over the waveband, or weighting the results over the waveband. This is necessary because of the spectral dependence of the molecular extinction coefficients within the waveband.
- C. The quantity of concern is calculated using both experimentally measured values and IRBLEM calculated values. For example, the total transmission could be calculated using the refractance and the molecular transmittance from IRBLEM, and the measured aerosol transmittance. In this case, the same measured aerosol transmittance would be used for both the primary and secondary images. A second example, would be the calculation of the aerosol transmittance using the measured total transmittance with the refractance and molecular transmittance calculated by IRBLEM.

In each case, Figs. 7-9a show the total band transmissions calculated using IRBLEM for the primary image (\diamond 's), the secondary image (Δ 's) when there is a mirage, and the total or sum of both images (\circ 's). It also shows the total obtained by using the ten measured aerosol transmittances for both the primary and secondary images instead of those calculated by IRBLEM (\blacksquare 's), and the transmissions measured by the transmissometer (\square 's). Figures 7-9b illustrate the differences between the measured and the model calculated transmissions (\circ 's for the actual measurements, and \blacksquare 's when the measured aerosols transmittances are substituted in place of those produced by IRBLEM). Figures 7-9c show the aerosol transmittances calculated by IRBLEM for both the primary image (\diamond 's) and the secondary image (Δ 's), the measured aerosol transmittances (\blacksquare 's), and those calculated using the molecular transmittance and refractance from IRBLEM with the measured total transmissions (\square 's). Figures 7-9d illustrate the differences between the measured and the calculated aerosol transmittances (\blacksquare 's for the actual measurements, and \circ 's when the measured transmissions are used). Figures 7-9e show the variation of the aerosol transmittances with visibility for the primary image (\diamond 's) and secondary image (Δ 's) calculated by IRBLEM for the measured aerosol transmittances (\blacksquare 's), for the calculation using the measured transmissions (\square 's), and a linear fit to this data. Figure 7f shows the calculated molecular transmittances using the weighting (weighted) function show in Fig. 3 (Δ 's) and using a uniform (average) weighting function (\square 's) as in Fig. 4. Figures 8f and 9f only show this for the average weighting function. Figures 7-9g show the variation of these same molecular

transmittances with respect to the relative humidity. Figures 7-9h illustrate the values for the refractance calculated by IRBLEM for both the primary (\square 's) and secondary (Δ 's) images. Zero-values indicate that the image doesn't exist. Figures 7-9i show the variation of these refractances with respect to the ASTD for both the primary (\diamond 's) and secondary (Δ 's) images. A second order fit to the primary image data is also shown on each graph.

5. DISCUSSION

5.1 MID IR OVER THE 7 KM PATH

Looking at Fig. 7a, one notices that the measured transmissions (\square 's) vary from 0.1 to 0.8, that those obtained using the measured aerosol transmittance (\blacksquare 's) range from 0.4 to 0.6, and that the model predicts total transmissions for the waveband ranging from 0.16 to 1.02! Three of the largest transmissions are predicted for the first week, during periods of negative ASTD, and coincide with the formation of secondary images (Δ 's). The addition of their intensity to that for the primary image is what significantly increases these transmissions by about 0.3 (or 50%). From Fig. 7b, one further notices that while the differences between the measured transmissions and the model predictions vary quite significantly about zero ($\sigma = 0.19$), the average of these differences is only 0.02. For the transmissions using the measured aerosol transmittance, the average difference is 0.09 ± 0.15 ($= \sigma$).

Figure 7c shows that the measured aerosol transmittances (\blacksquare 's) vary from 0.55 to 0.9, that those obtained using the measured transmission measurements (\square 's) range from 0.15 to 1.1, and that the NAM based model used within IRBLEM predicts transmittances ranging from 0.25 to 0.95 for the primary images. The predictions for the secondary images are generally about 0.05 less. From Fig. 7d, the average differences between the measurements and the predictions is 0.13 ± 0.22 , while that with the transmittances calculated using the measured transmissions is 0.04 ± 0.28 . Furthermore, comparing Figs. 7b and 7d, one notices that their highs and lows are very similar except that the differences calculated for the aerosol transmittances have a greater variance. Figure 7e shows that, in general, the measured and calculated aerosol transmittances increase as the measured visibility increases. A possible reason for the large scatter, in both Figs. 7d, 7e and 7b, may be due to the site at which the visibility was measured. As mentioned earlier, it was measured at the Subbase; however, this site is not necessarily representative of the visibility along the transmission path, and in particular near the midpoint of the path where the light rays are generally at their minimum elevation above the sea. Furthermore, this path is highly nonhomogeneous, particularly on the Coronado end, where there is a significant surf zone.

Figure 7f shows the variation of the predicted molecular transmittances over the mid IR waveband for both the weighted weighting function (Δ 's) and the average weighting function (\square 's). As can be seen, the values for the weighted function are always about 0.055 (~10%) greater than for the average function, and the transmittances only range from 0.67 to 0.75. Figure 7g shows that this slight variation is essentially due to changes in the relative humidity.

Finally, Fig. 7h shows the predicted values of the refractance for both primary and secondary images. The refractance for the primary images vary from 1.25 to 0.8, and as seen in Fig. 7i, this variation is essentially due to the air-sea temperature difference (ASTD). The refractance for the four cases where secondary images are predicted are about half the values for the respective primary images, and have no obvious dependence on the ASTD.

5.2 MID IR OVER THE 15 KM PATH

Looking at Fig. 8a, one notices that the measured transmissions (\square 's) vary from 0.02 to 0.18, that those obtained using the measured aerosol transmittance (\blacksquare 's) range from 0.01 to 0.14, and that the model predicts total transmissions for the waveband ranging from 0.0 to 0.2. The model also predicts nine cases where secondary images are expected, and three cases, during the first week, when the source should be below the horizon (transmission zero). However, while in one of the three cases there is good agreement, in the other two, the measured transmission is greater than 0.15. These are significant transmissions and when compared with some of the other data, indicates that rather than the source being below the transmissometer's horizon for these two cases, the transmissometer was probably seeing both a primary and secondary image of the source. From Fig. 8b, one discerns, that while the differences between the measured transmissions and the model predictions vary somewhat about zero ($\sigma = 0.03$), the average of these differences is only -0.02. For the transmissions using the measured aerosol transmittance, the average difference is 0.02 ± 0.05 . Furthermore, if not for several strong negative ASTDs during the first week, the variances would be even less.

Figure 8c shows that the measured aerosol transmittances (■'s) vary from 0.25 to 0.87, that those obtained using the measured transmission measurements (□'s) range from 0.05 to 0.6, and that the NAM based model predicts transmittances ranging from 0.08 to 0.9 for the primary images. Again, the predictions for the secondary images are generally about 0.05 less. From Fig. 8d, the average differences between the measurements and the predictions is 0.08 ± 0.25 , while that with the transmittances calculated using the measured transmissions is -0.13 ± 0.16 . Figure 8e shows that, in general, the measured and calculated aerosol transmittances increase as the measured visibility increases.

Figure 8f shows the variation of the predicted molecular transmittances over the mid IR waveband for the average weighting function (□'s). As can be seen, the transmittances only range from 0.17 to 0.20, and this slight variation is essentially due to changes in the relative humidity (see Fig. 8g).

Finally, Fig. 8h shows the predicted values of the refractance for both primary and secondary images. The refractance for the primary images vary from 1.55 to 0.0 (source below the horizon), and as seen in Fig. 8i, this variation is essentially due to changes in the ASTD; however, the spread of the points about the curve fit becomes much more significant once mirage formation occurs at sufficiently negative ASTD. One of the reasons for this is due to the high sensitivity which mirage (secondary image) formation has on the elevation heights of both the source and the receiver, and on the heights of the waves. In San Diego bay this is further complicated by the comings and goings of the tide. In fact, this is why no mirage is predicted on March 28th, for the 7 km path, when the ASTD is almost -4 °C. The refractance for the cases where secondary images are predicted are, again, about half the values for the respective primary images, and have no evident dependence on the ASTD. There are also three cases early in the week where the source is predicted to be below the horizon.

5.3 FAR IR OVER THE 15 KM PATH

Looking at Fig. 9a, one notices that the measured transmissions (□'s) vary from 0.00 to 0.20, that those obtained using the measured aerosol transmittance (■'s) range from 0.05 to 0.28, and that the model predicts total transmissions for the waveband ranging from 0.0 to 0.6. The model also predicts at least 14 cases where secondary images are expected, and four cases, during the first week, when the source should be below the horizon (transmission zero). Unfortunately, because of the switching schedule of the dual transmissometer, no measurements were made in the FIR at these times. From Fig. 9b, one notices that while the differences between the measured transmissions and the model predictions vary somewhat about zero ($\sigma = 0.06$), the average of these differences is only -0.04 . For the transmissions using the measured aerosol transmittance, the average difference is 0.02 ± 0.04 . Furthermore, as for the MIR case, if not for several strong negative ASTDs during the first week, the variances would again be less.

Figure 9c shows that the measured aerosol transmittances (■'s) vary from 0.6 to 0.95, that those obtained using the measured transmission measurements (□'s) range from 0.25 to 1.06, and that the NAM based model predicts transmittances ranging from 0.35 to 0.95 for the primary images. The predictions for the secondary images are generally about 0.05 less. From Fig. 9d, the average differences between the measurements and the predictions is 0.11 ± 0.18 , while that with the transmittances calculated using the measured transmissions is -0.10 ± 0.28 . Figure 9e shows that, in general, the measured and calculated aerosol transmittances increase as the measured visibility increases.

Figure 9f shows the variation of the predicted molecular transmittances over the mid IR waveband for the average weighting function (□'s). As can be seen the transmittances have a much greater range than for the MIR, varying from 0.07 to 0.32. Figure 9g illustrates that this variation is mostly due to changes in the relative humidity.

Finally, Fig. 9h shows the predicted values of the refractance for both primary and secondary images. The refractance for the primary images vary from 2.2 to 0.0 (source below the horizon), and as seen in Fig. 9i, this variation is essentially due to changes in the ASTD; however, as for the MIR case, the spread of the points about the curve fit becomes more significant once mirage formation occurs at sufficiently negative ASTD. The refractance for the cases where secondary images are predicted are, again, about half the values for the respective primary images, and show no dependence on the ASTD. There are also four cases early in the week where the source is predicted to be below the horizon.

6. CONCLUSIONS

An analysis is presented showing the effects of refraction, aerosol extinction, and molecular extinction on transmission

measurements obtained during the EO Propagation Assessment in Coastal Environments (EOPACE) campaign carried out in San Diego during March and April 1996. Infrared transmission measurements were made over both a 7 km path (mid IR) and a 15 km path (mid IR and far IR) at heights below 10 m above sea level (i.e., within the marine boundary layer). The average difference between all the measured transmissions and aerosol transmittances over the two paths with results obtained using the IR Boundary Layer Effects Model (IRBLEM) were found to be relatively small, even though the difference for individual measurements can be significant. The effect of molecular transmittance, as calculated using MODTRAN, is found to reduce the transmission by about 35% for the 7 km path, 72% for the mid IR over the 15 km path, and between 70% and 90%, depending upon the relative humidity, for the far IR over the 15 km path. The effect of aerosol transmittance, as calculated using a variation of the Navy Aerosol Model (NAM), is found to reduce the transmission from 10% to 90% for the mid IR over both the 7 and 15 km paths, and from 10% to 60% for the far IR over the 15 km path and seems to depend mostly upon the visibility. The effect of refractance, the focussing and defocussing of radiation due to atmospheric refraction, on the predicted transmissions is found to account for gains up to 20% and losses up to 20% for the 7 km path, and gains up to 100% and losses of 100% (source below the horizon) for the 15 km path. Losses in transmission are predicted for positive air-sea temperature differences (ASTDs), while gains are predicted for negative ASTDs if the source hasn't disappeared below the horizon (100% loss). Due to the importance of these effects and their dependence on different, though not necessarily completely independent, meteorological parameters, any IR transmission model for the marine boundary layer (MBL) must properly take the effects of molecular extinction, aerosol extinction, and refractance into account. Furthermore, due to the relative constant behaviour of the molecular transmittance compared to the high variability of the aerosol transmittance, and the sometimes dramatic effects produced by refractance, the total transmission can be thought of as fluctuating about the molecular transmittance with the fluctuations being controlled by the amount of aerosol in the MBL, and then being further refined by the air-sea temperature difference.

ACKNOWLEDGEMENTS

Special mention must be made acknowledging the efforts of Ken Davidson of the Naval Postgraduate School in Monterey, CA for his efforts in providing the two meteorological buoys, and to Douglas Jensen of NRaD, whose tireless efforts brought the EOPACE campaign to life.

REFERENCES

1. D. Dion and P. Schwering, "On the Analysis of Atmospheric Effects on Electro-Optical Sensors in the Marine Surface Layer", IRIS Conference, UK, June 1996.
2. A. Beck, L. S. Bernstein, D. C. Robertson, "MODTRAN: A Moderate Resolution Model for LOWTRAN 7", Final Report, Spectral Sciences, Inc., Burlington, MA, 1989.
3. P. Schwering and G. Kunz, "Infrared scintillation effects over sea", SPIE Proc., Vol. 2471, pp. 204-215, 1995.
4. S. G. Gathman, "Optical properties of the marine aerosol as predicted by the Navy Aerosol Model", Opt. Eng., Vol. 22(1), pp. 57-62, 1983.
5. G. de Leeuw, A.M.J. van Eijk, and G. R. Noordhuis, "Modeling aerosols and extinction in the marine atmospheric boundary layer", Proc. SPIE., Vol. 1968, pp. 70-80, 1993.
6. A.M.J. van Eijk and G. de Leeuw, "Modeling aerosol particle size distributions over the North Sea", Journal of Geophysical Research, Vol. 97C, pp. 14417-14429, 1992.
7. G. de Leeuw, "Modeling of extinction and aerosol backscatter profiles in the marine mixed layer", Applied Optics, Vol. 28, pp. 1356-1359, 1989.
8. W. T. Liu, K.B. Katsaros, and J.A. Businger, "Bulk Parametrization of Air-Sea Exchanges of Heat and Water Vapor Including the Molecular Constraints at the Interface", Journal of Atmospheric Sciences, Vol. 36, pp. 1722-1735, 1979.
9. J. L. Forand, "The L(W)WKD Marine Boundary Layer Model", DREV R-9618, March, 1997, UNCLASSIFIED.
10. A. S. Monin and A. M. Obukhov, "Basic Regularity in Turbulent Mixing in the Surface Layer of the Atmosphere", Trad. Geophys. Inst. ANSSSR, No. 24, p. 163, 1954.
11. A. Blanchar, "Phase and intensity ray tracing to study the propagation of coherent radiation in the atmosphere and other media", DREV R-4699, 1993, UNCLASSIFIED.
12. C.R. Zeisse, S.G. Gathman, A.N. de Jong, G. de Leeuw, J.L. Forand, D. Dion and K.L. Davidson, "Low Elevation transmission measurements at EOPACE part I: molecular and aerosol effects", SPIE Proc., Vol. 3125, 1997.
13. A.N. de Jong, G. de Leeuw and K.L. Davidson, "Low elevation transmission measurements at EOPACE part III: scintillation effects", SPIE Proc., Vol. 3125, 1997.

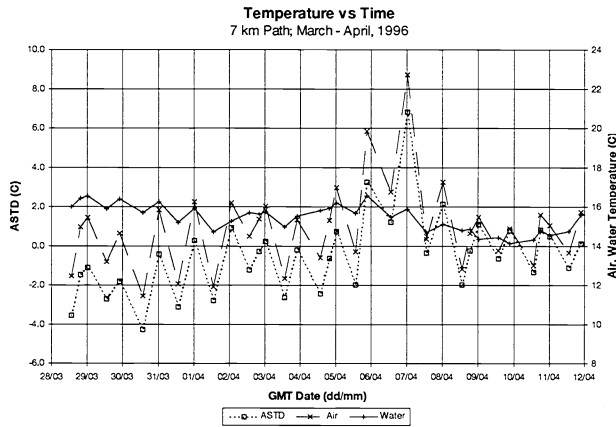


Figure 5a - Air and water temperatures measured by the “Mean” buoy, and the resultant ASTD for the 7 km path during the IOP.

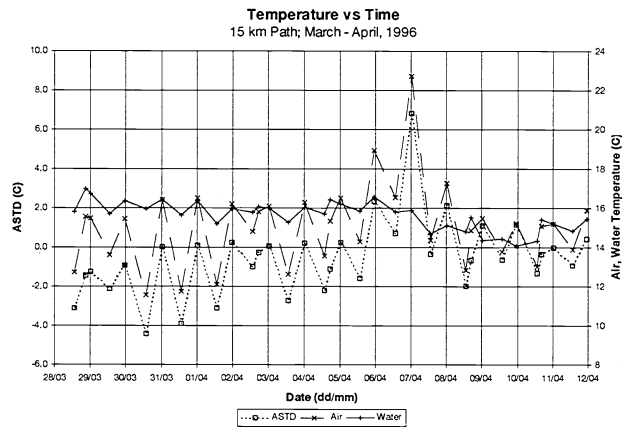


Figure 6a - Air and water temperatures measured by the “Flux” buoy, and the resultant ASTD for the 15 km path during the IOP.

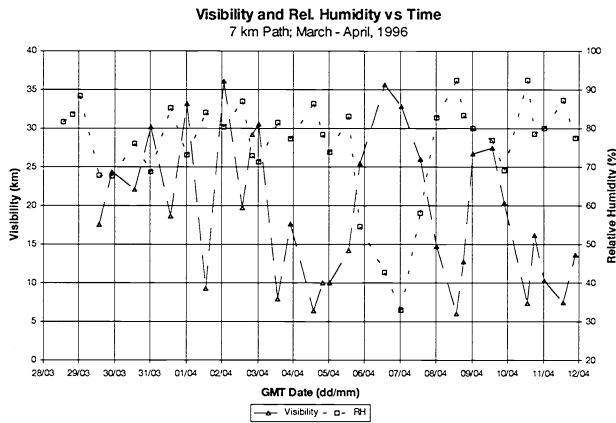


Figure 5b - Visibility and the relative humidity for the 7 km path during the IOP.

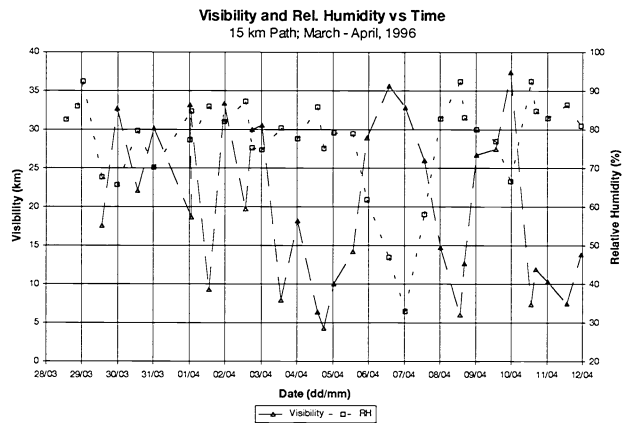


Figure 6b - Visibility and the relative humidity for the 15 km path during the IOP.

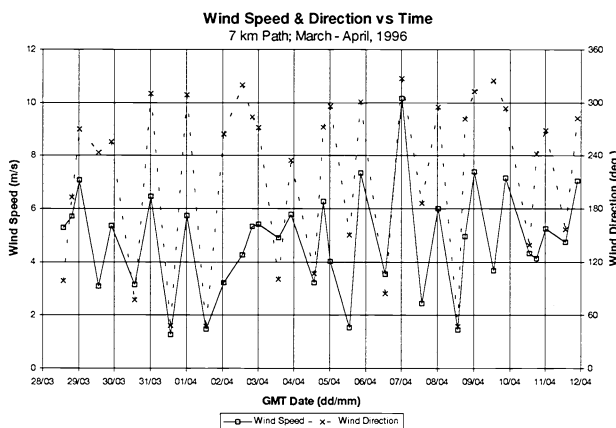


Figure 5c - Wind speed and direction for the 7 km path during the IOP.

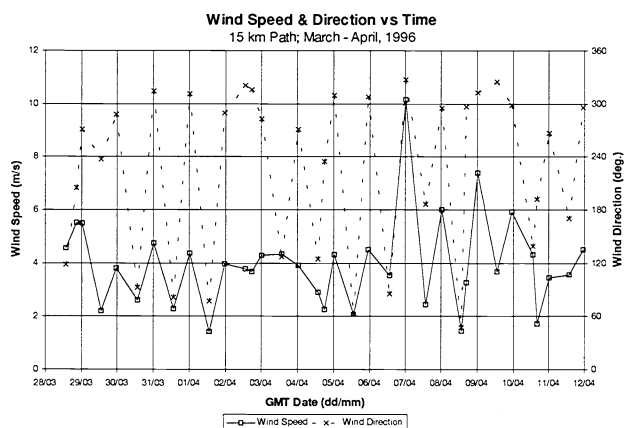


Figure 6c - Wind speed and direction for the 15 km path during the IOP.

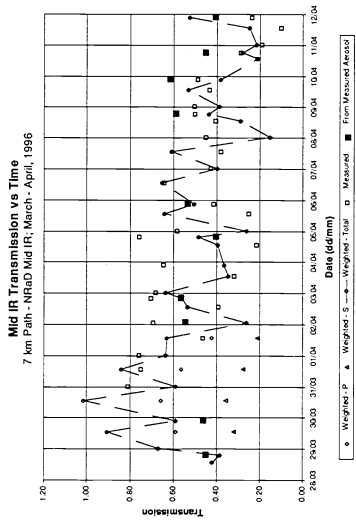


Figure 7a - Mid IR transmission calculations and measurements for the 7 km path.

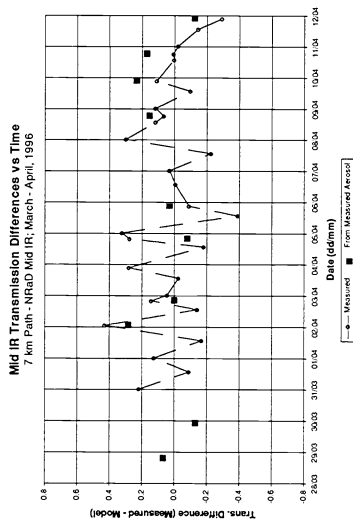


Figure 7b - Differences between measured and calculated transmissions in the mid IR for the 7 km path.

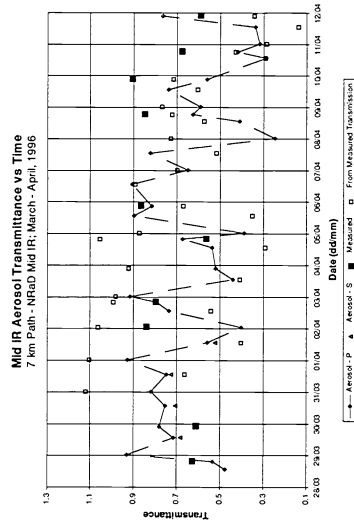


Figure 7c - Mid IR aerosol transmittance calculations and measurements for the 7 km path.

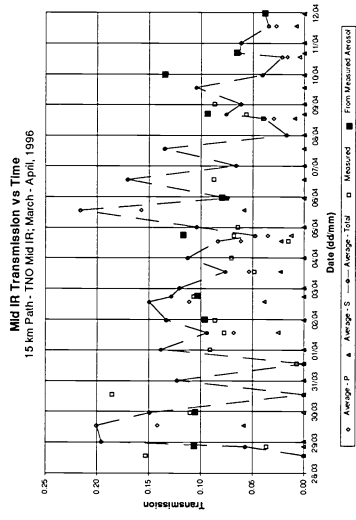


Figure 8a - Mid IR transmission calculations and measurements for the 15 km path.

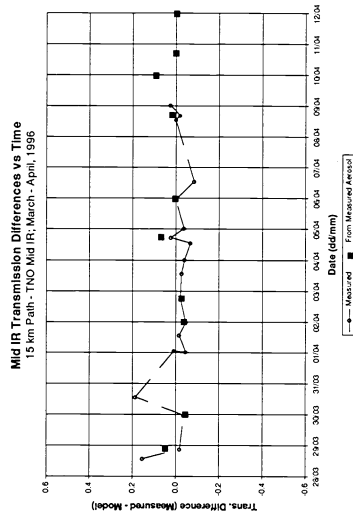


Figure 8b - Differences between measured and calculated transmissions in the mid IR for the 15 km path.

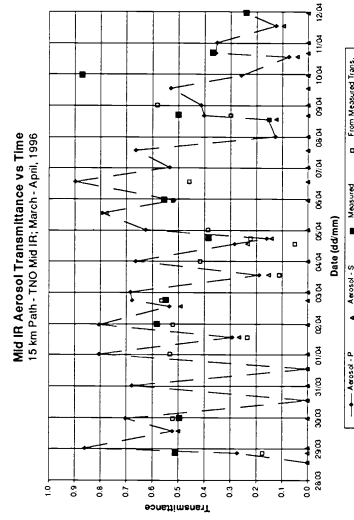


Figure 8c - Mid IR aerosol transmittance calculations and measurements for the 15 km path.

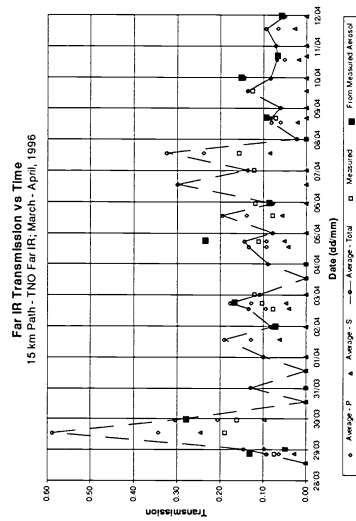


Figure 9a - Far IR transmission calculations and measurements for the 15 km path.

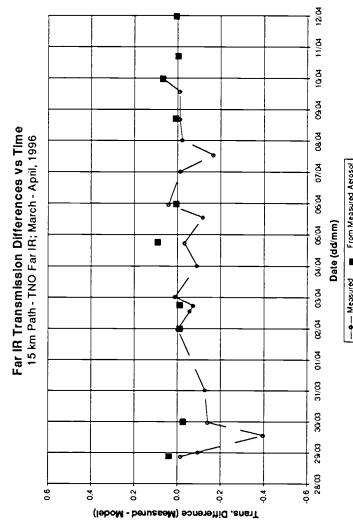


Figure 9b - Differences between measured and calculated transmissions in the far IR for the 15 km path.

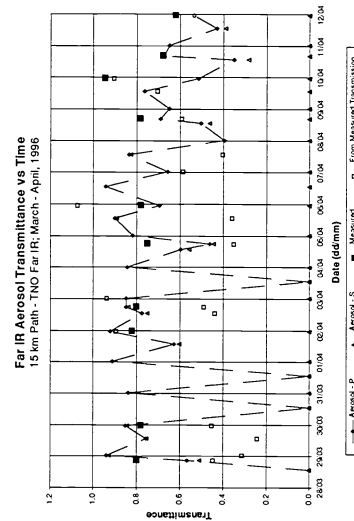


Figure 9c - Far IR aerosol transmittance calculations and measurements for the 15 km path.

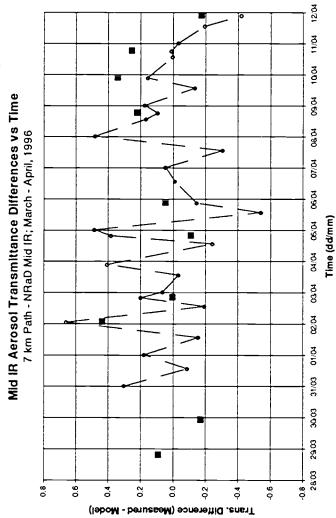


Figure 7d - Differences between measured and calculated mid IR aerosol transmittances for the 7 km path.

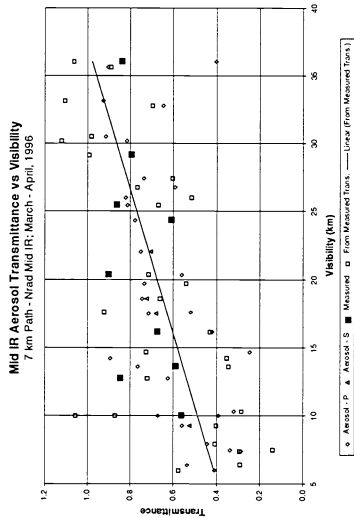


Figure 7e - Mid IR measured and calculated aerosol transmittances versus the visibility for the 7 km path.

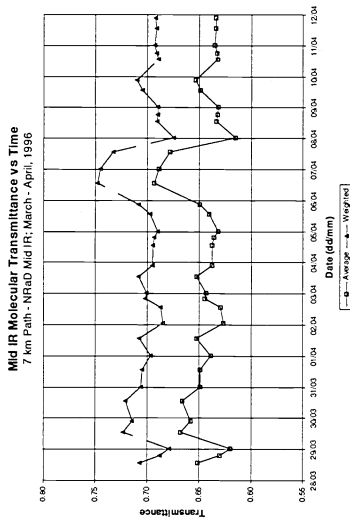


Figure 7f - Mid IR molecular transmittance for the 7 km path calculated using MODTRAN.

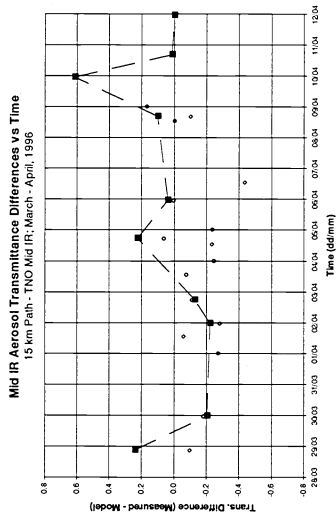


Figure 8d - Differences between measured and calculated mid IR aerosol transmittances for the 15 km path.

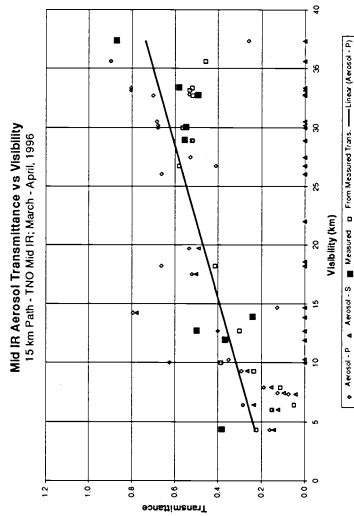


Figure 8e - Mid IR measured and calculated aerosol transmittances versus the visibility for the 15 km path.

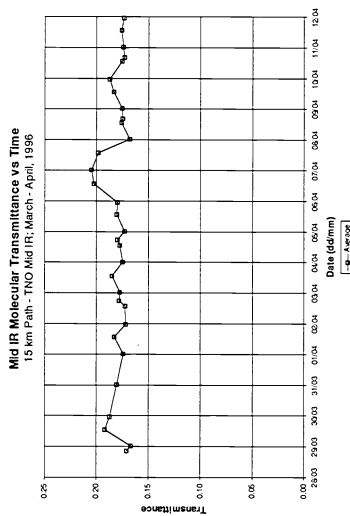


Figure 8f - Mid IR molecular transmittance for the 15 km path calculated using MODTRAN.

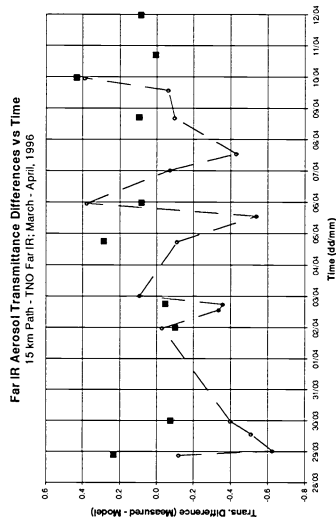


Figure 9d - Differences between measured and calculated far IR aerosol transmittances for the 15 km path.

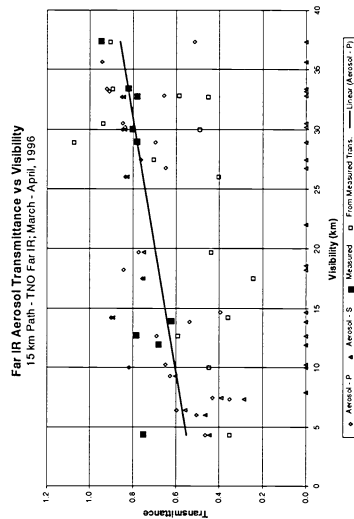


Figure 9e - Far IR measured and calculated aerosol transmittances versus visibility for the 15 km path.

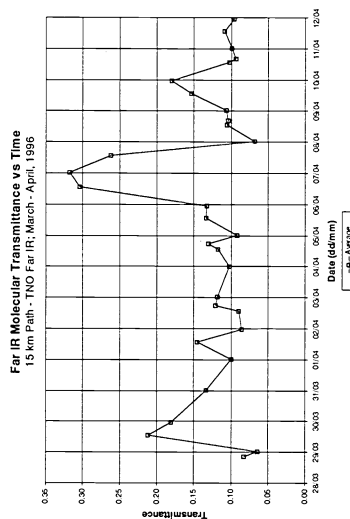


Figure 9f - Far IR molecular transmittance for the 15 km path calculated using MODTRAN.

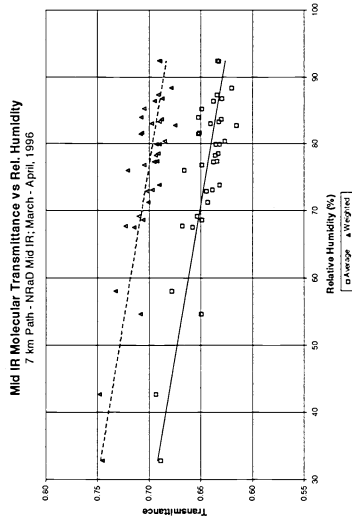


Figure 7g - Mid IR molecular transmittance calculations versus rel. humidity for the 7 km path.

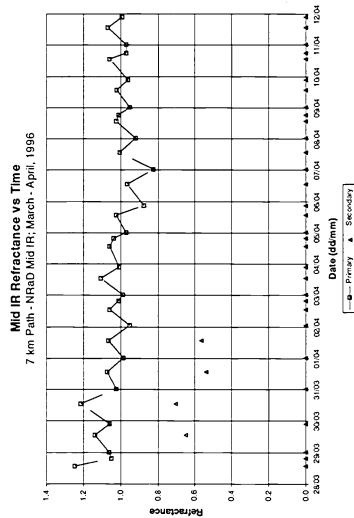


Figure 7h - Mid IR refractance calculations for primary and secondary images over the 7 km path.

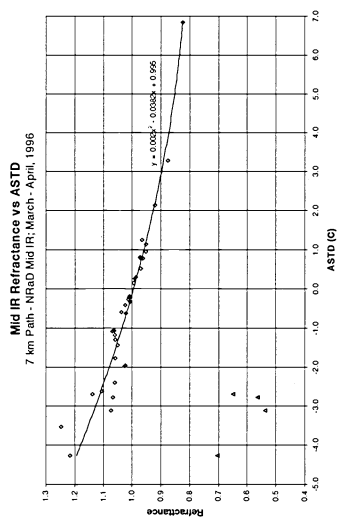


Figure 7i - Mid IR refractance calculations versus ASTD for the 7 km path.

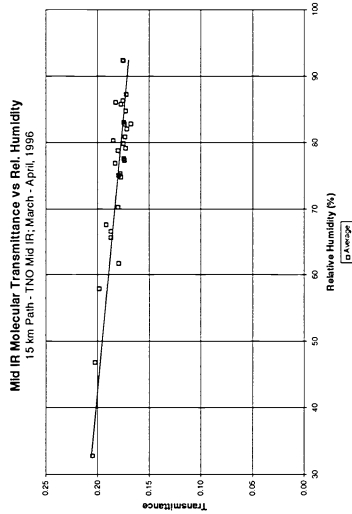


Figure 8g - Mid IR molecular transmittance calculations versus relative humidity for the 15 km path.

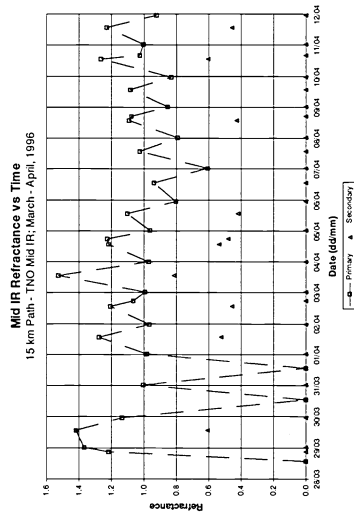


Figure 8h - Mid IR refractance calculations for primary and secondary images over the 15 km path.

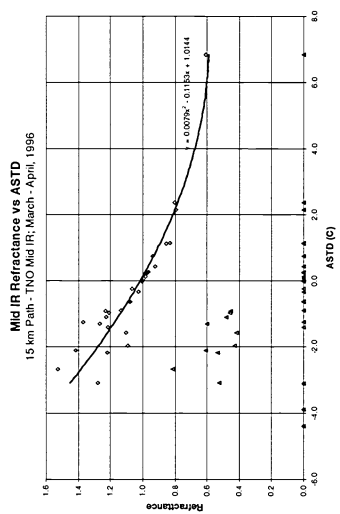


Figure 8i - Mid IR refractance calculations versus ASTD for the 15 km path.

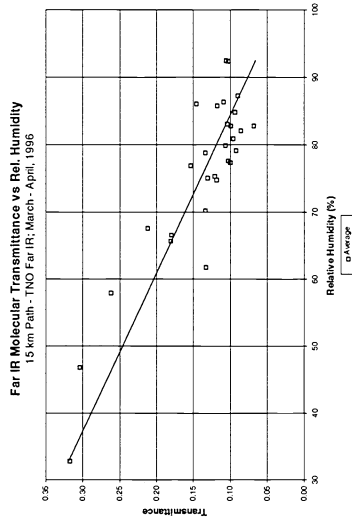


Figure 9g - Far IR molecular transmittance calculations versus relative humidity for the 15 km path.

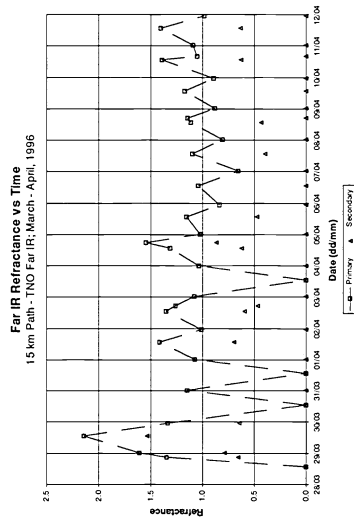


Figure 9h - Far IR refractance calculations for primary and secondary images over the 15 km path.

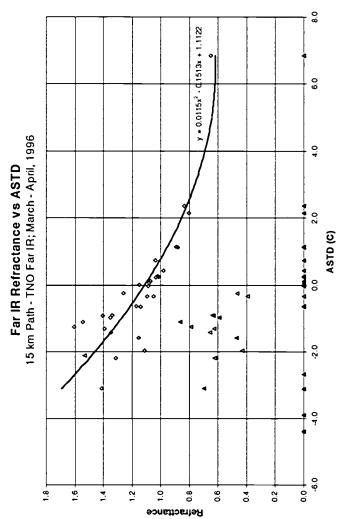


Figure 9i - Far IR refractance calculations versus ASTD for the 15 km path.